Electronic Supplementary Material (ESI) for Inorganic Chemistry Frontiers.


# Supporting Information

## Electron-deficient Co Modulated by Constructing Heterojunction Co@NC Boosting Electroreduction of Nitrate to Ammonium

Bo Zhang,[a] Fengshou Yu,[a] Yaohua Hong,[a] Yuzhuo Zhou,[a] Yaheng Wang,[a] Shaobo Zhang[a] and Lu-Hua Zhang [a, *]

[a] National-Local Joint Engineering Laboratory for Energy Conservation in Chemical Process Integration and Resources Utilization, School of Chemical Engineering and Technology, Hebei University of Technology, Tianjin 300130, P. R. China.

*Corresponding authors e-mail address: luhuazhang@hebut.edu.cn

**Table of Contents**

Fig. S1. SEM image of Co@NC-4.

Fig. S2. SEM and image of Co@C.

Fig. S3. XPS spectra of Co@C, Co@NC-0.5, Co@NC-1, Co@NC-2 and Co@NC-4.

Table S1. Elemental analysis results of Co@NC-x samples.

Table S2. Cobalt contents, as determined by ICP analysis.

Fig. S4. UPS spectra of Co@C and Co@NC-4.

Fig. S6. LSV curves of Co@C, Co@NC-0.5, Co@NC-1, Co@NC-2 and Co@NC-4.

Fig. S6. Ultraviolet absorption and concentration-absorbance calibration curves of $NH_3$.

Fig. S7. Ultraviolet absorption and concentration-absorbance calibration curves of $NO_3^-$.

Fig. S8. Ultraviolet absorption and concentration-absorbance calibration curves of $NO_2^-$.

Fig. S9. FE of $NH_3$, $H_2$ and $NO_2^-$ productions with Co@C, Co@NC-0.5, Co@NC-1, Co@NC-2 and Co@NC-4.

Fig. S10. FE of $NH_3$, $H_2$ and $NO_2^-$ productions with Co@NC-6 and Co@NC-8; Yield rate of $NH_3$ of each catalyst.

Fig. S11. CV curves at various scan rates of Co@C, Co@NC-0.5, Co@NC-1, Co@NC-2 and Co@NC-4.

Fig. S12. The corresponding Cdl and ECSA normalized current densities of Co@C, Co@NC-0.5, Co@NC-1, Co@NC-2 and Co@NC-4 samples.

Fig. S13. XRD patterns, Co 2p XPS spectra and N 1s XPS spectra of Co@NC-4 before and after electrolysis at -0.5 V.

Fig. S14. $^1H$ NMR spectra of the electrolyte after the $NO_3^-$ reduction at -0.5 V for 2 h.

Fig. S15. Modeling and atomic structure of reaction intermediates for Co@NC-4 and Co@C.

Fig. S16. $N_2$ adsorption-desorption isotherms and pore-size distributions of Co@NC-4 and Co@C.

Table S3. Comparison of $NH_3$ selectivity and yield rate by electrocatalytic nitrate reduction.

**Materials.** Cobalt nitrate hexahydrate ($Co(NO_3)\cdot 6H_2O$, 99%), terephthalic acid (TPA, 99%), triethylene diamine (TEDA, 98%) and urea ($CO(NH_2)_2$, 99%) were obtained from Shanghai Macklin Biochemical Co. Melamine (98%), N, N-Dimethylformamide (DMF, AR), and ethanol absolute ($C_2H_5OH$, AR) were obtained from Shanghai Aladdin Biochemical Technology Co. Nafion solution (5 wt.%) was obtained from Sigma-Aldrich. All chemicals and solvents were received and used without further purification. All aqueous solutions were prepared with MilliQ ultrapure water (18.2 MΩ.cm).

**Characterization.** The ultraviolet-visible (UV-vis) absorbance of ion concentrations was gained with TU-1900. X-ray diffraction (XRD) data was accomplished on a JEMARM300F microscope. Scanning electron microscope (SEM) was carried out with Czech TESCAN MIRA LMS. The Raman spectra were recorded on a LabRam HR Evolution (Horiba) Raman spectrometer. Fourier transform infrared (FTIR) transmittance spectra were derived by Thermo Scientific Nicolet iS20. UPS spectra were achieved by PHI5000 VersaProbe III (Scanning ESCA Microprobe) SCA (Spherical Analyzer). $^1$H NMR were obtained by the isotope labeling experiments on a BRUKER AVANCE 400.

**Theoretical simulation.**

The DFT calculations were performed by Vienna Ab initio Simulation Package (VASP) with the projector augmented wave (PAW) method. The generalized gradient approximation (GGA) of Perdew-Burke-Ernzerhof (PBE) functional was applied to treat the exchange-functional. The energy cutoff for the plane wave basis expansion was set to 400 eV and the force on each atom less than -0.02 eV/Å was set for convergence criterion of geometry relaxation. To prevent interaction between periodic structures, a vacuum of 15 Å was added along the z direction. The Brillouin zone integration is treated using 1×3×1 k-point sampling. The self-consistent calculations apply a convergence energy threshold of 10-6 eV.

The free energies of the $NO_3RR$ were calculated by the equation:

$$\Delta G = \Delta E_{DFT} + \Delta E_{ZPE} - T\Delta S$$

where ΔEDFT represents the DFT electronic energy difference of every steps. The corrections for zero-point energy (ΔEZPE) and entropy variation (ΔS) were obtained through VASPKIT. The calculations were performed at a temperature of T = 298.15 K.

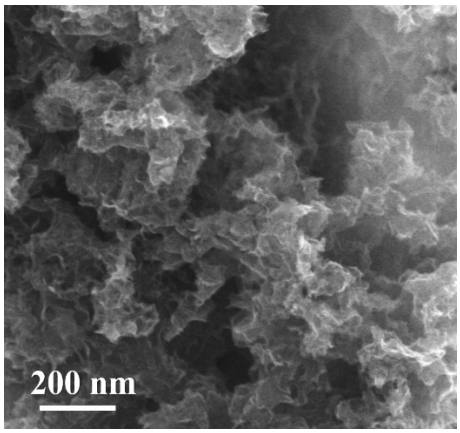


**Fig. S1.** SEM image of Co@NC-4.

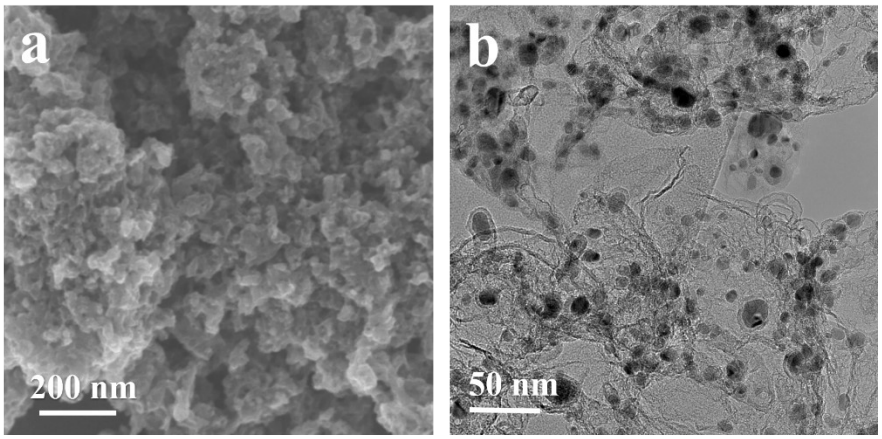


**Fig. S2.** (a) SEM and (b)TEM image of Co@C.

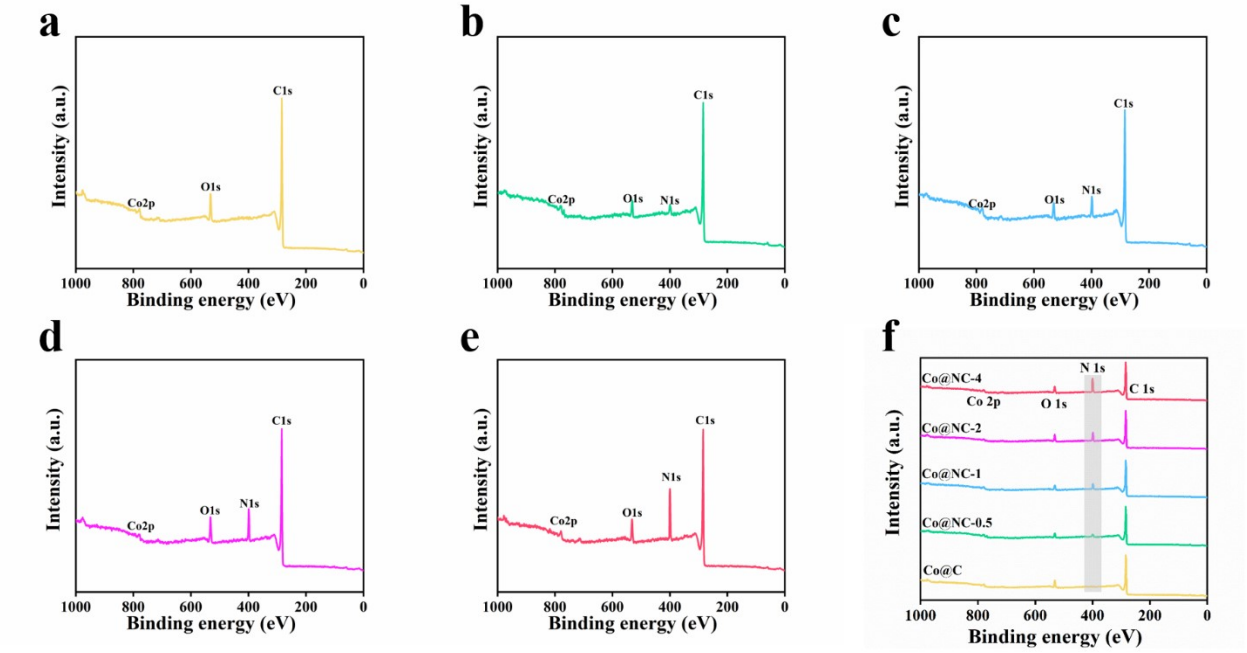


**Fig. S3.** XPS survey spectra of (a) Co@C, (b) Co@NC-0.5, (c) Co@NC-1, (d) Co@NC-2 and (e) Co@NC-4. (f) xps general spectra.

**Table S1.** Elemental analysis results of Co@NC-x samples.

| Sample | Co (wt. %) | N (wt. %) | C (wt. %) |
|---|---|---|---|
| Co@C | 7.62 | 0.09 | 82.4 |
| Co@NC-0.5 | 6.77 | 0.93 | 80.4 |
| Co@NC-1 | 6.89 | 2.05 | 73.14 |
| Co@NC-2 | 7.01 | 4.92 | 67.33 |
| Co@NC-4 | 6.27 | 8.41 | 79.45 |
| Co@NC-6 | 6.38 | 7.92 | 70.24 |

**Table S2.** Cobalt contents, as determined by ICP analysis.

| Sample | Co (wt. %) |
|---|---|
| Co@C | 12.86 |
| Co@NC-0.5 | 11.43 |
| Co@NC-1 | 11.77 |
| Co@NC-2 | 11.42 |
| Co@NC-4 | 11.90 |
| Co@NC-6 | 11.74 |

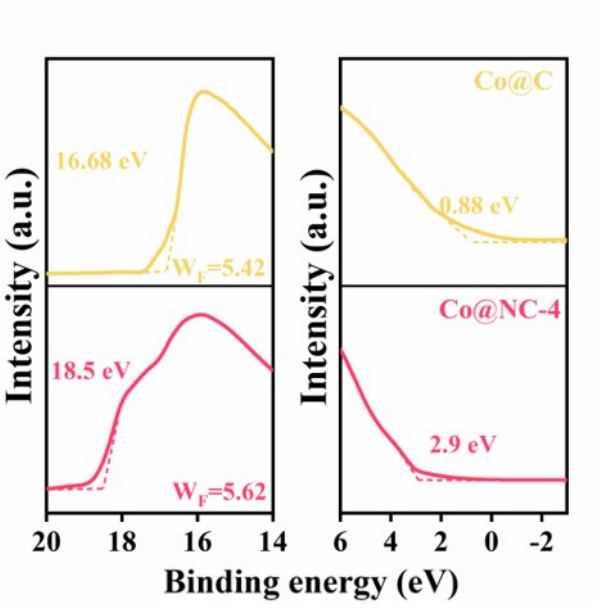


**Fig. S4**. UPS spectra of Co@C and Co@NC-4.

The sample of Co@C shows a lower work function of 5.42 eV, than that for Co@NC-4 (5.62 eV), suggesting that more electrons were transferred to NC upon doping with N (Fig. 2).

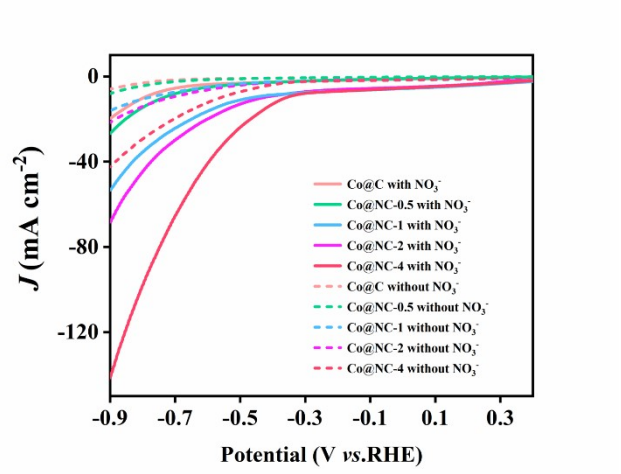


**Fig. S5.** LSV curves of Co@C and Co@NC-x in 0.5 M $Na_2SO_4$ and 0.1 M $NO_3^-$ (pH=11.5)

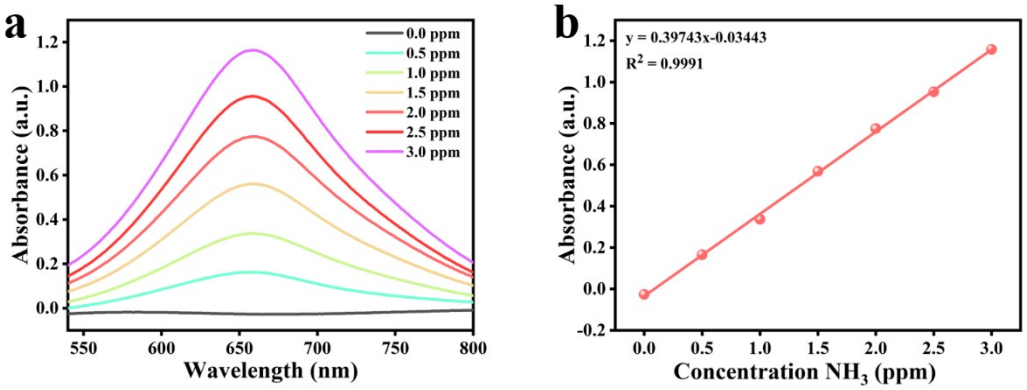


**Fig. S6.** (a) Ultraviolet absorption and (b) concentration-absorbance calibration curves of $NH_3$.

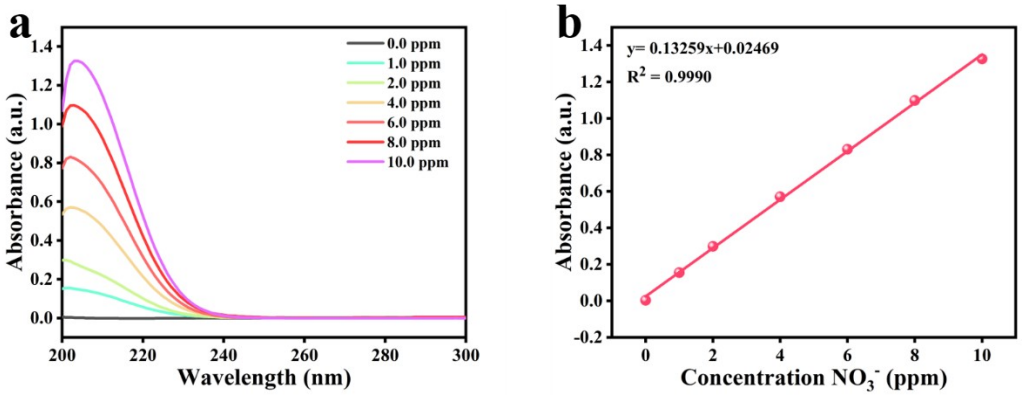


**Fig. S7.** (a) Ultraviolet absorption and (b) concentration-absorbance calibration curves of $NO_3^-$.

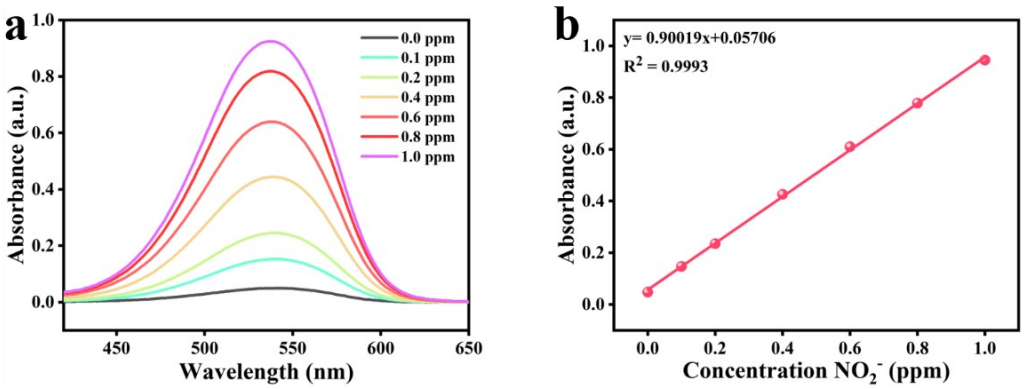


**Fig. S8.** (a) Ultraviolet absorption and (b) concentration-absorbance calibration curves of $NO_2^-$.

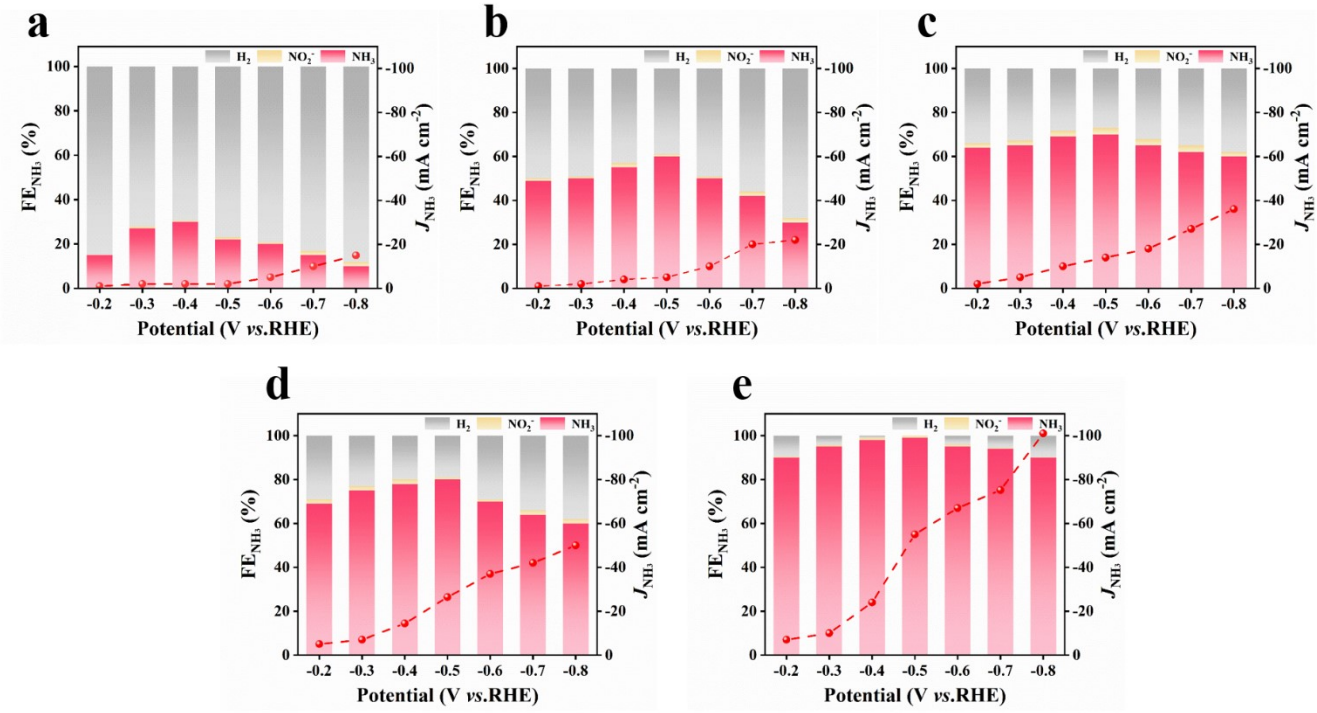


**Fig. S9.** FE of $NH_3$, $H_2$ and $NO_2^-$ productions with (a) Co@C, (b) Co@NC-0.5, (c) Co@NC-1, (d) Co@NC-2 and (e) Co@NC-4.

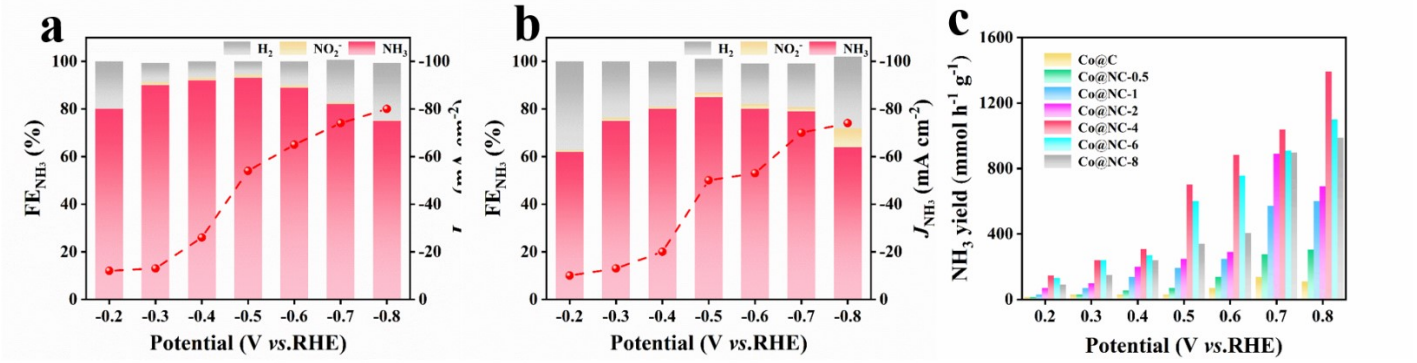


**Fig. S10.** FE of $NH_3$, $H_2$ and $NO_2^-$ productions with (a) Co@NC-6 and (b) Co@NC-8; (c) Yield rate of $NH_3$

of each catalyst.

The doping of $g$-$C_3N_4$was further increased to prepare Co@NC-6 and Co@NC-8. Comparison of the performances revealed that increasing the $g$-$C_3N_4$ doping did not further improve the Faraday efficiency, current density and yield of the catalysts. This corresponds to the previous characterization that further increasing the g-C3N4 doping did not increase the nitrogen loading of the catalyst.

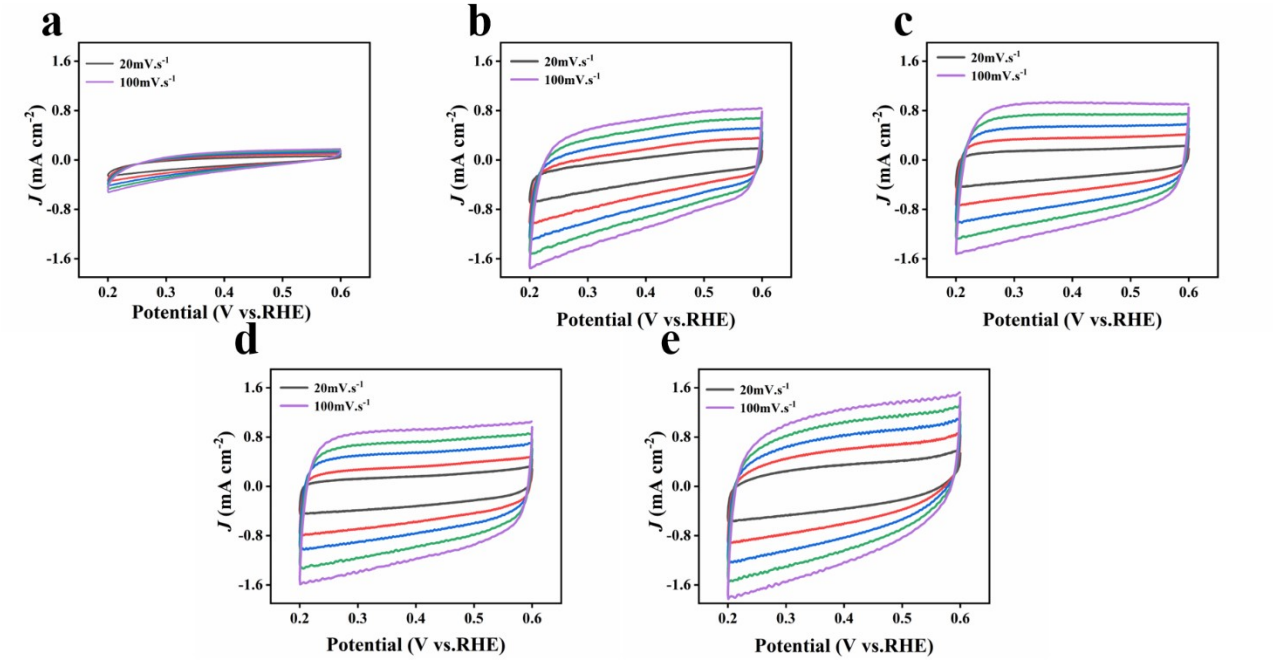


**Fig. S11.** CV curves at various scan rates of (a) Co@C, (b) Co@NC-0.5, (c) Co@NC-1, (d) Co@NC-2 and (e) Co@NC-4.

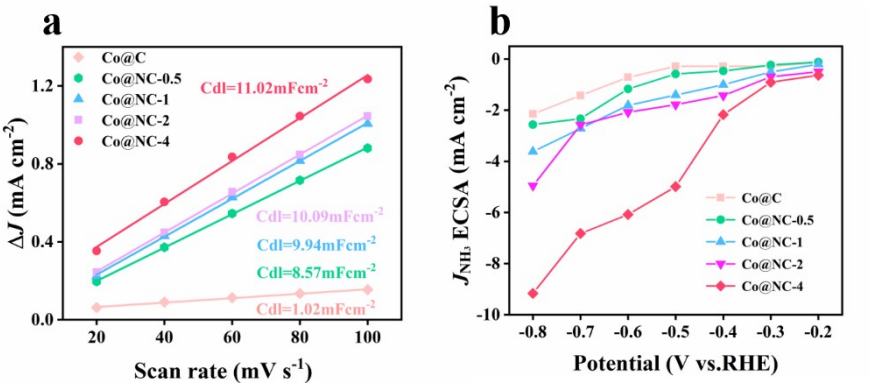


**Fig. S12.** (a) The corresponding $C_{dl}$ by ECSA of Co@C and Co@NC-x samples. (b) ECSA normalized current densities for $NH_3$ formation.

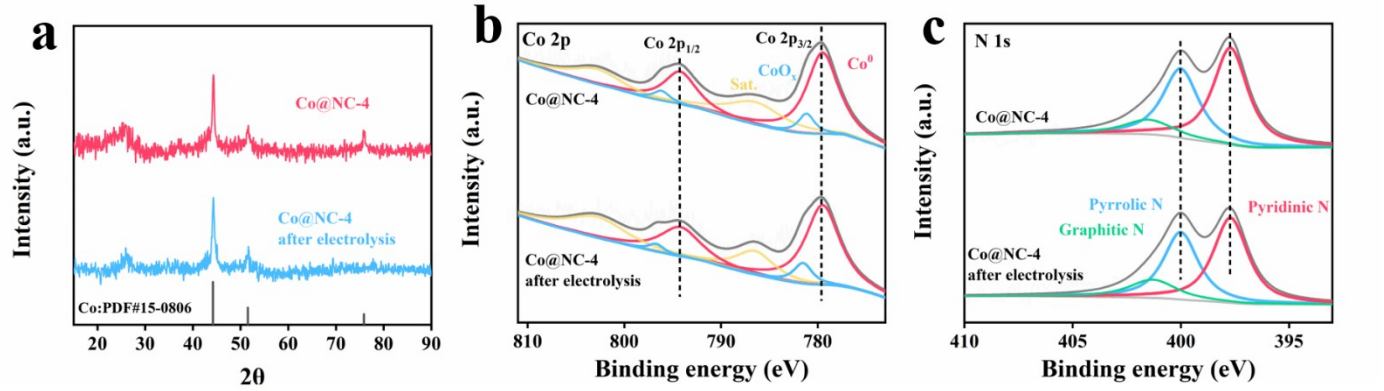


**Fig. S13.** XRD patterns (a) , Co 2p XPS spectra (b) and N 1s XPS spectra (c) of Co@NC-4 before and after electrolysis at -0.5 V.

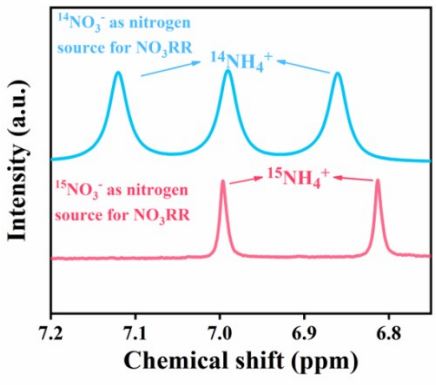


**Fig. S14.** $^{1}H$ NMR spectra of the electrolyte after the $NO_3^-$ reduction at -0.5 V for 2 h with $^{14}NaNO_3^-$ and $^{15}NaNO_3^-$ as N-source, respectively.

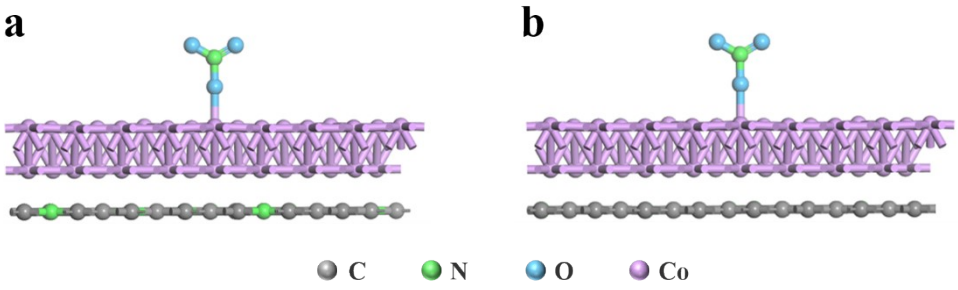


**Fig. S15.** Modeling and atomic structure of reaction intermediates for (a) Co@NC-4 and (b) Co@C.

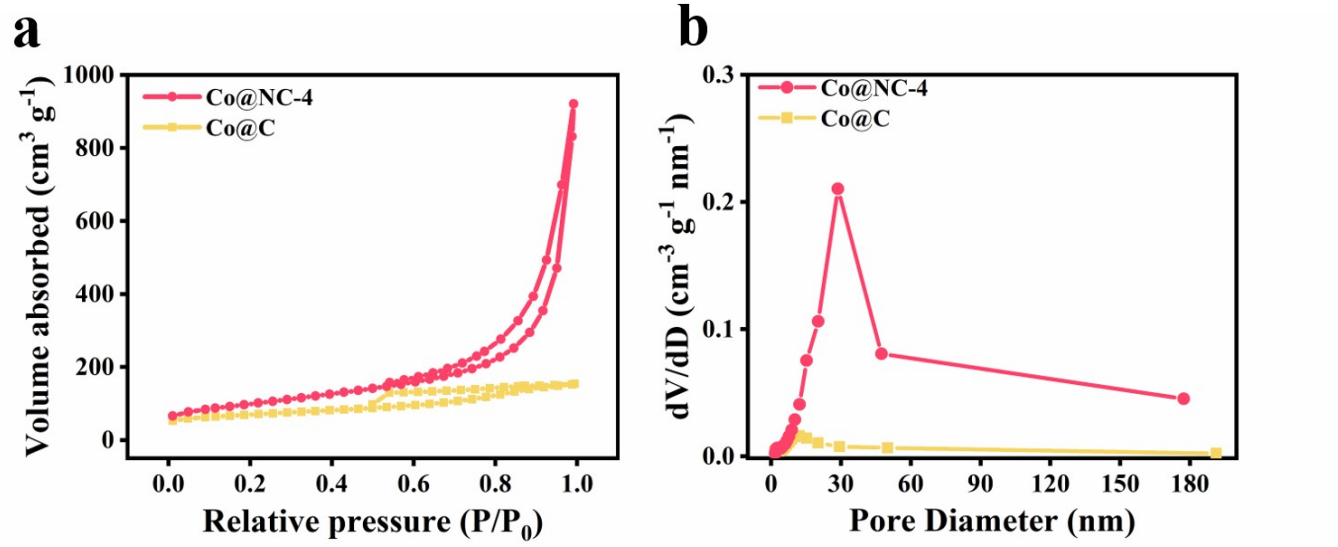


**Fig. S16.** (a) $N_2$ adsorption-desorption isotherms and (b) pore-size distributions of Co@NC-4 and Co@C.

Co@NC-4 has a larger specific surface area compared to Co@C, while Co@C has a pore size of around 30 nm.

**Table S3.** Comparison of $NH_3$ selectivity and yield rate by electrocatalytic nitrate reduction.

| Catalysts | Electrolyte | $FE_{NH3}$ (%) | Potential | $NH_3$ yield (mmol $h^{-1}$ $g_{cat}^{-1}$) | Ref. |
|---|---|---|---|---|---|
| **Co@NC-4** | **0.1 M $NaNO_3$, 0.5 M $NaSO_4$ (PH=11.5)** | **99.1** | **-0.5 V** | **1392.8** | **This work** |
| Cu-$Co_3O_4$ | 500 ppm $NO_3^-$, 0.1 M $NaSO_4$ | 86.5 | -0.6 V *vs*. RHE | 36.71 | 1 |
| CoNi@NC | 1 M KOH, 0.1 M $KNO_3$ | 93 | -0.1 V *vs*. RHE | 168 | 2 |
| Bi-NC | 0.5 M KOH, 0.05 M $KNO_3$ | 88.7 | -0.35 V *vs*. RHE | 81.17 | 3 |
| $Ru_1Cu_{10}$/rGO | 1 M KOH, 0.1 M $KNO_3$ | 98 | -0.02 V vs. RHE | 240 | 4 |
| Pd/C | 0.1 M NaOH, 20 mM $NO_3^-$ | 35 | -0.2 V *vs*. RHE | 17.04 | 5 |
| $CuCo_2O_4$/CF | 1 M KOH, 0.1 M $KNO_3$ | 81.9 | -0.3 V *vs*. RHE | 394.5 | 6 |
| $Fe_2Ti_2O_5$NFs | PBS, 0.1 M $NaNO_3$ | 87.6 | -0.9 V *vs*. RHE | 730 | 7 |

| | | | | | |
|---|---|---|---|---|---|
| $Fe_2M$ | 0.05 M $H_2SO_4$, 0.05 M $KNO_3$ | 90.55 | -1.1 V *vs*. RHE | 1211.76 | 8 |
| Zn/Cu-2.3 | 0.5 M $K_2SO_4$, 0.01 M $KNO_3$ | 92.56 | / | 96 | 9 |
| Fe SAC | 0.1 M $K_2SO4$, 0.5 M $KNO_3$ | 67 | -0.85 V *vs*. RHE | 1176.5 | 10 |
| In-S-G | 0.1 M KNO, 1 M KOH | 75 | -0.5 V *vs*. RHE | 220 | 11 |
| Cu@C | 1 M KOH, 0.1 M $KNO_3$ | 72 | -0.3 V *vs*. RHE | 27.58 | 12 |
| Cu-$N_4$ | 0.1 M KOH, 0.1 M $KNO_3$ | 84.7 | -0.1 V *vs*. RHE | 735.3 | 13 |
| Ru/$Co(OH)_2$ | 1 M KOH, 0.1 M $KNO_3$ | 98.78 | 0.01 V *vs*. RHE | 1430 | 14 |
| Ru/Ni | 1 M KOH, 0.1 M $NaNO_3$ | 97 | -0.1 V *vs*. RHE | 384.1 | 15 |
| NTCDA-LIG | 1 M $NaNO_3$ | 83.7 | -0.94 V *vs*. RHE | 328.4 | 16 |

**References**


1. Z. Niu, S. Fan, X. Li, Z. Liu, J. Wang, J. Duan, M. O. Tadé and S. Liu, Facile Tailoring of the Electronic Structure and the d-Band Center of Copper-Doped Cobaltate for Efficient Nitrate Electrochemical Hydrogenation, *ACS Appl. Mater. Interfaces,* 2022, **14**, 35477-35484.
2. F. Lei, Y. Zhang, M. Xu, K. Li, M. Zhang, R. Huai, J. Xie, P. Hao, G. Cui and B. Tang, Energy-Efficient Ammonia Synthesis from Nitrate via CoNi Alloys Incorporated in Carbon Frameworks, *ACS Sustain. Chem. Eng.*, 2023, **11**, 9057-9064.
3. W. Zhang, S. Zhan, J. Xiao, T. Petit, C. Schlesiger, M. Mellin, J. P. Hofmann, T. Heil, R. Müller, K. Leopold and M. Oschatz, Coordinative Stabilization of Single Bismuth Sites in a Carbon–Nitrogen Matrix to Generate Atom-Efficient Catalysts for Electrochemical Nitrate Reduction to Ammonia, *Adv. Sci.*, 2023, **10**, 2302623.
4. W. Gao, K. Xie, J. Xie, X. Wang, H. Zhang, S. Chen, H. Wang, Z. Li and C. Li, Alloying of Cu with Ru Enabling the Relay Catalysis for Reduction of Nitrate to Ammonia, *Adv. Mater.*, 2023, **35**, 2202952.
5. J. Lim, C.-Y. Liu, J. Park, Y.-H. Liu, T. P. Senftle, S. W. Lee and M. C. Hatzell, Structure Sensitivity of Pd Facets for Enhanced Electrochemical Nitrate Reduction to Ammonia, *ACS Catal.*, 2021, **11**, 7568-7577.
6. Z. Niu, S. Fan, X. Li, P. Wang, Z. Liu, J. Wang, C. Bai and D. Zhang, Bifunctional copper-cobalt spinel electrocatalysts for efficient tandem-like nitrate reduction to ammonia, *Chem. Eng. J.*, 2022, **450**, 138343.
7. H. Du, H. Guo, K. Wang, X. Du, B. A. Beshiwork, S. Sun, Y. Luo, Q. Liu, T. Li and X. Sun, Durable Electrocatalytic Reduction of Nitrate to Ammonia over Defective Pseudobrookite $Fe_2TiO_5$ Nanofibers with Abundant Oxygen Vacancies, *Angew. Chem. Int. Ed.*, 2023, **62**, e202215782.

8. Y. Lv, S.-W. Ke, Y. Gu, B. Tian, L. Tang, P. Ran, Y. Zhao, J. Ma, J.-L. Zuo and M. Ding, Highly Efficient Electrochemical Nitrate Reduction to Ammonia in Strong Acid Conditions with $Fe_2$M-Trinuclear-Cluster Metal–Organic Frameworks, *Angew. Chem. Int. Ed.*, 2023, **62**, e202305246.
9. L. Wu, J. Feng, L. Zhang, S. Jia, X. Song, Q. Zhu, X. Kang, X. Xing, X. Sun and B. Han, Boosting Electrocatalytic Nitrate-to-Ammonia via Tuning of N-Intermediate Adsorption on a Zn−Cu Catalyst, *Angew. Chem. Int. Ed.*, 2023, **62**, e202307952.
10. Z.-Y. Wu, M. Karamad, X. Yong, Q. Huang, D. A. Cullen, P. Zhu, C. Xia, Q. Xiao, M. Shakouri, F.-Y. Chen, J. Y. Kim, Y. Xia, K. Heck, Y. Hu, M. S. Wong, Q. Li, I. Gates, S. Siahrostami and H. Wang, Electrochemical ammonia synthesis via nitrate reduction on Fe single atom catalyst, *Nat. Comm.*, 2021, **12**.
11. F. Lei, W. Xu, J. Yu, K. Li, J. Xie, P. Hao, G. Cui and B. Tang, Electrochemical synthesis of ammonia by nitrate reduction on indium incorporated in sulfur doped graphene, *Chem. Eng. J.*, 2021, **426**, 131317.
12. Z. Song, Y. Liu, Y. Zhong, Q. Guo, J. Zeng and Z. Geng, Efficient Electroreduction of Nitrate into Ammonia at Ultralow Concentrations Via an Enrichment Effect, *Adv. Mater.*, 2022, **34**, 2204306.
13. J. Yang, H. Qi, A. Li, X. Liu, X. Yang, S. Zhang, Q. Zhao, Q. Jiang, Y. Su, L. Zhang, J.-F. Li, Z.-Q. Tian, W. Liu, A. Wang and T. Zhang, Potential-Driven Restructuring of Cu Single Atoms to Nanoparticles for Boosting the Electrochemical Reduction of Nitrate to Ammonia, *J. Am. Chem. Soc.*, 2022, **144**, 12062-12071.
14. W. Zhu, F. Yao, Q. Wu, Q. Jiang, J. Wang, Z. Wang and H. Liang, Weakened d–p orbital hybridization in in situ reconstructed Ru/β-Co(OH)2 heterointerfaces for accelerated ammonia electrosynthesis from nitrates, *Energy Environ. Sci.*, 2023, **16**, 2483-2493.
15. F. Zhou and C. Sun, Nitrate-to-Ammonia Conversion on Ru/Ni Hydroxide Hybrid through Zinc-Nitrate Fuel Cell, *Small*, 2022, **18**, 2200436.
16. L. Cheng, T. Ma, B. Zhang, L. Huang, W. Guo, F. Hu, H. Zhu, Z. Wang, T. Zheng, D.-T. Yang, C.-K. Siu, Q. Liu, Y. Ren, C. Xia, B. Z. Tang and R. Ye, Steering the Topological Defects in Amorphous Laser-Induced Graphene for Direct Nitrate-to-Ammonia Electroreduction, *ACS Catal.*, 2022, **12**, 11639-11650.